Received: 25 November 2022 | Revised: 25 April 2023 | Accepted: 8 May 2023

DOI: 10.33012/navi.604

ORIGINAL ARTICLE

Atom Strapdown: Toward Integrated Quantum Inertial Navigation Systems

Benjamin Tennstedt*[1] | Ashwin Rajagopalan[2] | Nicolai B. Weddig[1] | Sven Abend[2] | Steffen Schön[1] | Ernst M. Rasel[2]

[1] Institut für Erdmessung, Leibniz University Hannover, Lower Saxony, Germany

[2] Institut für Quantenoptik, Leibniz University Hannover, Lower Saxony, Germany

Correspondence
Benjamin Tennstedt
Email: tennstedt@ife.uni-hannover.de

Abstract

We present an alternative technique for estimating the response of a cold atom interferometer (CAI). Using data from a conventional inertial measurement unit (IMU) and common strapdown terminology, the position of the atom wave packet is tracked in a newly introduced sensor frame, enabling hybridization of both systems in terms of acceleration and angular rate measurements. The sensor frame allows for an easier mathematical description of the CAI measurement and integration into higher-level navigation systems. The dynamic terms resulting from the transformation of the IMU frame into the CAI sensor frame are evaluated in simulations. The implementation of the method as a prediction model in an extended Kalman filter is explained and demonstrated in realistic simulations, showing improvements of over two orders of magnitude with respect to the conventional IMU strapdown solution. Finally, the implications of these findings for future hybrid quantum navigation systems are discussed.

Keywords

atom interferometry, hybridization, inertial navigation, sensor fusion

1 | INTRODUCTION

Atom interferometry is a highly precise technique for inertial sensing (Kasevich et al., 1991). By interrogating a free-evolving atom wave packet with a series of laser pulses, information about accelerations and turn rates can be extracted, allowing the calculation of a complete navigation solution (position, velocity, and attitude). Applications of this technique for accelerometers (Barrett et al., 2014), gyroscopes (Gauguet et al., 2009; Schubert et al., 2021), and complete inertial measurement units (IMUs) (Gebbe et al., 2021; Gersemann et al., 2020) based on Bose–Einstein condensates are currently under research. The potential position accuracy reaches 5 m after 1 h of inertial navigation (Jekeli, 2005), which makes atom interferometry a highly promising technique for navigation in global navigation satellite system (GNSS)-denied environments.

Commercial options are already available for static settings, i.e., quantum gravimeters (Vermeulen et al., 2018), and have an accuracy and long-term stability comparable or even superior to those of other high-end conventional sensors

(Freier et al., 2016). In the case of changing inertial quantities, some challenges still remain. The atom interferometer itself has a very limited dynamic range when used alone, and conventional measurement models for the interferometer readout are often not suited for highly dynamic trajectories. Thus, in state-of-the-art techniques, hybridization with other sensors, such as conventional accelerometers, is mandatory in order to produce a navigation solution (Cheiney et al., 2018; Richardson et al., 2020; Templier et al., 2022; Zahzam et al., 2022).

In our prior work (Tennstedt & Schön, 2020), a combination of conventional IMUs and atom interferometers in the frame of an extended Kalman filter (EKF) was presented. The phase shift of the cold atom interferometer (CAI) is predicted from the measurement of the conventional IMU, determining the target fringe of the CAI and effectively solving the fringe ambiguity problem. The CAI measurement is then used to correct the prediction model of the IMU, which enables the estimation of a number of IMU error quantities, e.g., sensor bias or misalignment, based on the state vector configuration (Tennstedt & Schön, 2021) This model has been successfully tested with two IMUs of different accuracies, with the higher-class IMU emulating an atom interferometer (Weddig et al., 2021). With the bias of the conventional IMU corrected, the position drift of the combined navigation solution was reduced by a factor of 30. In general, the combined solution benefits from the superior long-term stability of the CAI, as discussed in Tennstedt et al. (2021). This solution was further evaluated for applications on low Earth orbit satellites (HosseiniArani et al., 2022), where the electrostatic accelerometer in use has a lower white noise density than the CAI, but a larger long-term drift.

However, the models introduced thus far have been developed under the assumption that the atom interferometer is aligned with the body frame of the vehicle. In addition, the equations are not scalable, which prevents the integration of one or more atom interferometers in a higher-level navigation system. In this paper, a suitable coordinate system for the sensor frame is introduced in order to allow an easier integration in future high-level navigation and multi-sensor systems. First, a system is developed for a general case with several sensor frames, followed by a special CAI multi-axis scheme based on differential measurements presented in Gersemann et al. (2020). This multi-axis scheme is then used for further evaluation in the scope of this paper.

The remainder of this paper is structured as follows. The measurement principle of CAIs for inertial sensing is briefly summarized in Section 2. The necessity and basic idea for hybridization are explained, and two types of hybridization that are relevant for this paper are described. In Section 3, the mathematical framework for the phase shift prediction, the *atom strapdown* scheme, is developed. A comparison with a second existing hybridization scheme follows in Section 3.2. Performance studies are carried out in Section 4 based on simulations, where the phase shift is of particular focus. Based on realistic dynamics derived from measurement campaigns, the single phase shift terms are quantified and visualized in order to gain insight and derive requirements for future hybrid sensor designs. Furthermore, the error of the predicted phase shift with respect to the CAI observation is tracked and discussed. The conclusions of this work are presented in Section 5 with a final evaluation.

2 | ATOM INTERFEROMETRY FOR INERTIAL SENSING

Atom interferometers use the wave-particle characteristics of an atomic wave packet to deduce inertial quantities. In a basic Mach–Zehnder-type configuration,

shown in Figure 1, an atomic wave packet is manipulated by a series of three directed laser pulses in order to split, reverse, and recombine the internal states of the atoms.

During the interaction of the atom wave packet with the beam splitter lasers, the atoms are set in a superposition of two internal energy states, $|1, m\rangle$ and $|2, m + k\hbar\rangle$, where m is the momentum of the wave packet, $\hbar$ is the reduced Planck constant, and $k = \frac{4\pi}{\lambda}$ is the effective laser wave number, which itself is related to the wavelength λ, e.g., 780 nm for rubidium. The probability that the atoms are in one of the two states oscillates with a certain *Rabi* frequency Ω_{eff} and depends on the time of the laser interaction, the pulse time τ. If the atoms are all in state 1 at the beginning of the interaction, they will all switch their state after a certain 2τ pulse into state 2, resembling a mirror pulse. Likewise, if the interaction lasts for a duration of τ, the probability for a transition is 50% and a *state*-splitter pulse can be realized. During each atom–laser interaction, a phase shift between the two states is accumulated because both states yield different momenta. Under a number of assumptions such as a symmetric pulse sequence (Antoine & Borde, 2003), it is sufficient to describe the position of the center of mass of the atoms at the *mid-point line* between both states, as shown in Figure 1. The phase shift between the two states then depends on the relative position x of the atoms in the sensor frame, as well as the effective wave number k of the lasers for each atom–laser interaction. The main limitation of this method is that the trajectories of the two atomic states must overlap at the time of the recombination pulse. This requirement might be violated in the presence of rotations, where a loss of contrast attributed to an insufficient closing of the wave packet trajectory occurs (Roura et al., 2014) and a *separation phase* must be considered.

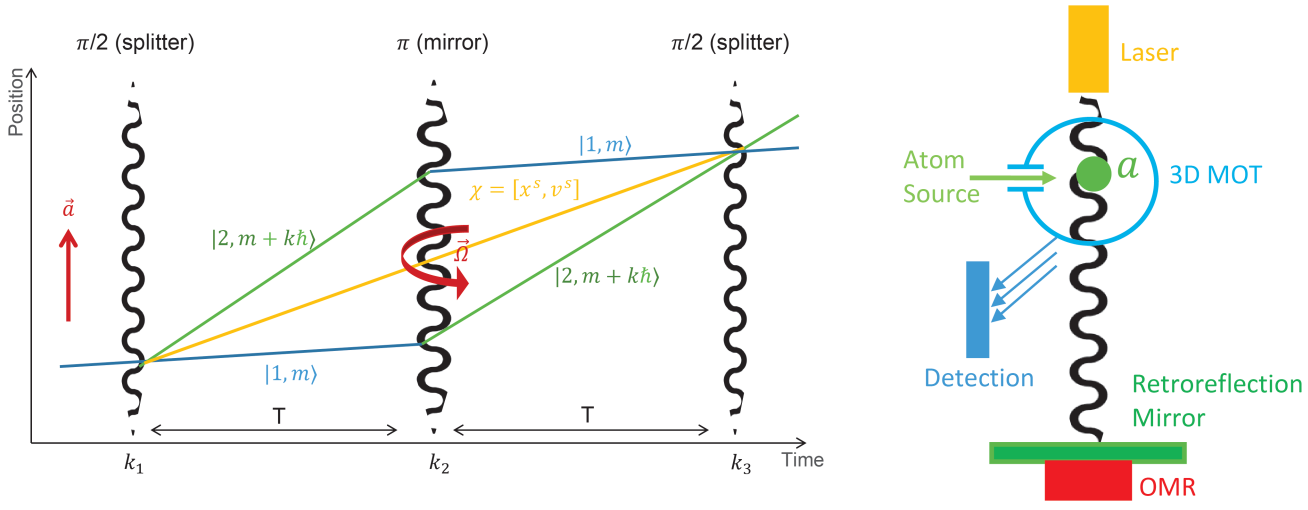

FIGURE 1 Basic principle of a CAI

Left: Atom interferometry in the Mach–Zehnder configuration. An atomic wave packet is manipulated by directed laser pulses with a separation time T, allowing inertial quantities to be extracted from the resulting phase shift. The atom position along the mid-point line (yellow) is decisive for the resulting phase shift. Right: Scheme of a CAI. After leaving their source, the atoms a are prepared in a three-dimensional magneto-optical trap (MOT). Afterwards, they are launched into free propagation, and their states are manipulated by a series of laser pulses. Finally, the atoms in one of the states are counted by detecting photons that are emitted after additional manipulation steps. A retroreflection mirror is used in order to allow Raman state transitions (Kasevich & Chu, 1992) and acts as a spatial phase reference. In this setup, an optomechanical resonator (OMR) is used to measure the mirror vibrations, i.e., frame accelerations, and to reconstruct the interferometer phase.

For the introduced three-pulse Mach–Zehnder configuration and under consideration of the midpoint-line theorem, the final phase shift $\phi(t_3)$ at the time t_3 of the last interaction reads as follows:

$$\phi(t_3) = k_1 x(t_1) - 2k_2 x(t_2) + k_3 x(t_3) \tag{1}$$

The actual observation after a measurement cycle is the transition probability, or population, of the atoms. This population p can be assessed by counting the number of atoms in one of the two states, N_1 or N_2. In turn, the population can be related back to the phase shift via the following relation:

$$p = \frac{N_1}{N_1 + N_2} = \frac{1}{2}(1 + \cos\phi) \tag{2}$$

As a didactic example, the phase shift can now be calculated by the inverse cosine. To retrieve the inertial effects from the phase shift, additional models are needed. Assuming a constant acceleration a, a simple motion equation of $x = \frac{1}{2}at^2$ is sufficient. The quantity of interest can then be computed by applying the model to Equation (1), plugging the result into Equation (2), and then solving for a. The final equation for the inertial quantity in this example is then:

$$a = \frac{1}{kT^2}\arccos(2p - 1) \tag{3}$$

if $k = k_1 = k_2 = k_3$ (static setting) and T is the interrogation time between the laser pulses, cf., Figure 1.

The approach of using the inverse cosine shows one major drawback of the CAI. The phase shift is only defined in the interval of $0 \leq \phi \leq \pi$, which is a flank of the cosine function. For a typical setup with an interrogation time of 10 ms and the example above, this range corresponds to an acceleration of only approximately 2 mm/s^2. A vibration of the sensor frame may be larger than this value, which leads to ambiguity in the CAI measurement.

This drawback can be circumvented by either compensating for vibrations via a stabilized platform or using different acceleration sensors to measure the vibration and to combine the signals via convolution with the CAI response function, cf., Cheiney et al. (2018) or Richardson et al. (2020), in order to enable measurements with the atom interferometer.

Another way to benefit from the better long-term stability of the CAI is to use a conventional IMU as the main sensor and to correct any drift errors with the atom interferometer measurement, e.g. Tennstedt & Schön (2020), while the solution of the ambiguity problem works in a similar manner. Both techniques will be explained in the next section.

3 | HYBRIDIZATION

The idea behind hybridization is driven by two objectives. The first objective is to resolve the fringe ambiguity. This is done by reconstructing the atom interferometer phase with the help of high-rate sensors able to resolve signals that would otherwise exceed the dynamic range of the interferometer. For this step, we propose the *atom strapdown* technique as a prediction method that utilizes acceleration and angular rate measurements from an IMU as input.

The second objective is to correct the IMU-based prediction model with the observation of the atom interferometer. To this end, an EKF is applied with the bias of the accelerometers and gyroscopes as a state augmentation.

In the following subsections, this formalism is described, compared with another phase reconstruction method that has been previously applied to experimental data, and finally implemented in the framework of an EKF.

3.1 | Phase Reconstruction with Atom Strapdown

As clarified in the introduction, the phase shift of an atom interferometer primarily depends on the relative position of the atom wave packet in the sensor frame. The basic equations of a typical strapdown algorithm that is used to compute the kinematic state of a moving platform from accelerometer and gyroscope measurements are adapted in order to estimate the wave packet position and its velocity.

3.1.1 | Sensor Frame Phase Shift Representation

To allow a more general three-degree-of-freedom formalism, the position vector pointing to the center of the atom wave packet a in an arbitrary sensor frame s with index $j \in [x, y, z]$ will be denoted as $\mathbf{x}^{sj}_{sj,a}$. For now, it is assumed that each CAI has only one sensitive direction, defined by its effective wave vector $\mathbf{k}^{sj}$. As an example, for $j = x$, cf., Figure 2, the vector may read $\mathbf{k}^{sx} = [k, 0, 0]^T$, where k is the effective wave number introduced above. The phase shift ϕ^{sj} in the corresponding sensor frame can then be calculated by Equation (1). The origin of the s-frame is defined in the exact location at which the atom wave packet is released into free propagation. When the first splitter pulse is applied at $t_1 = 0$, the initial position in the respective sensor frame is zero, and hence, the phase shift according to Equation (1) is reduced to two terms:

$$\phi^{sj} = -2\mathbf{k}^{sj} \cdot \mathbf{x}^{sj}_{sj,a}(t = T) + \mathbf{k}^{sj} \cdot \mathbf{x}^{sj}_{sj,a}(t = 2T) \tag{4}$$

where T is the interrogation time between the laser pulses and $\cdot$ denotes a scalar product.

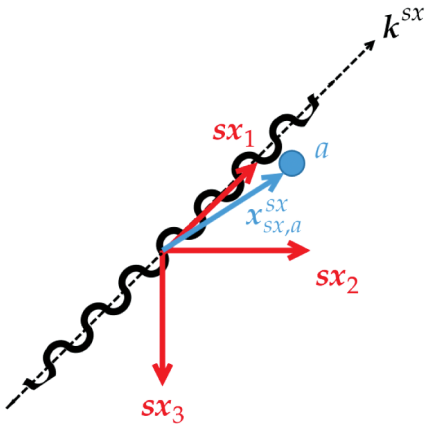

FIGURE 2 Position vector $\mathbf{x}^{sx}_{sx,a}$ pointing to the atom wave packet in the CAI sensor frame *sx* The axis $\mathbf{sx}_1$ corresponds to the forward direction. In this case, the forward direction is aligned with the beam splitter laser field and, thus, the sensitive axis $\mathbf{k}^{sx}$ of the sensor, indicated by the black dotted line. For the other two axes, $\mathbf{sx}_3$ aligned in the downward direction orthogonal to $\mathbf{sx}_1$, and $\mathbf{sx}_2$ completes the right-handed system.

If an IMU is used to estimate the position of the atom wave packets in the sensor frame, a framework known from inertial navigation can be utilized: the strapdown algorithm. The differential motion equations for the position $\mathbf{x}_{sj,a}^{sj}$ and velocity $\mathbf{v}_{sj,a}^{sj}$ of the respective atom wave packets are as follows:

$$\dot{\mathbf{x}}_{sj,a}^{sj} = \mathbf{v}_{sj,a}^{sj} \tag{5}$$

$$\dot{\mathbf{v}}_{sj,a}^{sj} = -\left(\mathbf{f}_{i,sj}^{sj} - 2\Omega_{i,sj}^{sj}\mathbf{v}_{sj,a}^{sj}\right) + \mathbf{g}^{sj} \tag{6}$$

Here, $\mathbf{f}_{i,sj}^{sj}$ are the specific forces, i.e., accelerations, and the term $2\Omega_{i,sj}^{sj}\mathbf{v}_{sj,a}^{sj}$ denotes the Coriolis force, as the atoms have a velocity relative to the s-frame. The gravity vector $\mathbf{g}^{sj}$ is considered as well. The rotation rates are expressed in the skew-symmetric matrix $\Omega_{i,sj}^{sj} = [\omega_{i,sj}^{sj}\times]$, where the index i denotes the inertial frame. The index sj with $j \in [x, y, z]$ denotes the corresponding sensor frame, cf., Figure 3. As an example, the vector $\mathbf{v}_{sx,a}^{sx}$ marks the velocity between the sx frame origin and the atom wave packet a in the sx frame, expressed in the sx frame.

Note that the equations are solved in the respective s-frame; hence, the change in the velocity $\dot{\mathbf{v}}_{sj,a}^{sj}$ of the atom with respect to the s-frame points in the direction opposite to the acceleration of the s-frame, cf., Equation (6). This does not account for gravity $\mathbf{g}^{sj}$, which affects the motion of the atom wave packet even when the s-frame is not accelerated. Gravity can be considered as an external force. Additional effects, such as centrifugal and Euler accelerations, that depend on the position $\mathbf{x}_{sj,a}^{sj}$ are not considered in this study, as their effects are comparably small for short interrogation times. For future actual implementations with specified CAI parameters, such as the initial position of the atoms in the s-frame, the differential equation (Equation (6)) can be enhanced accordingly. Furthermore, the recoil velocity caused by the laser–atom interaction is neglected, as the impact on the phase shift is small compared with the effect of the accelerations.

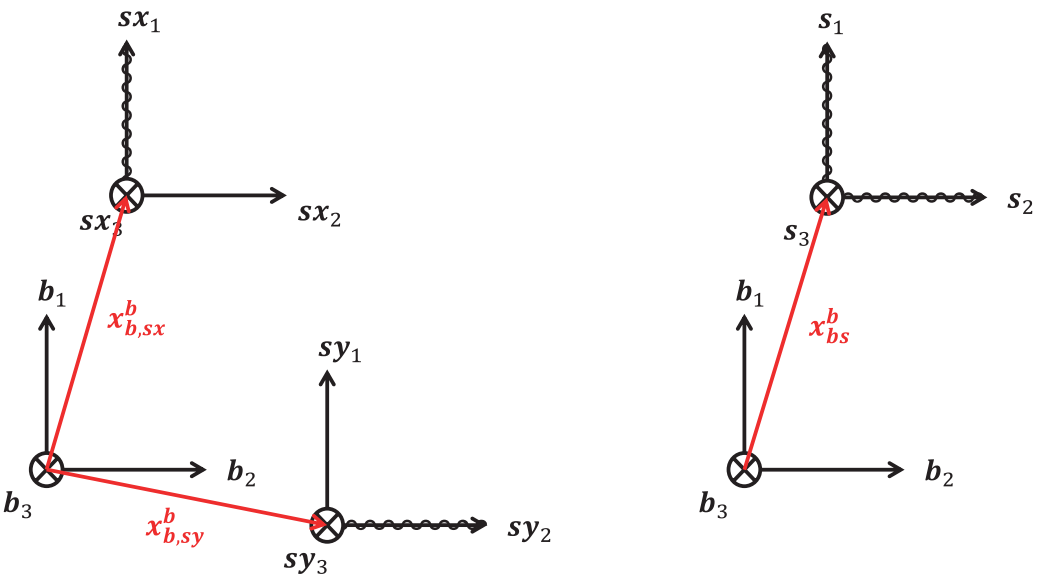

FIGURE 3 Sensor frames as defined in the strapdown model
All systems are right-handed. The b-frame is the center of the platform, corresponding to the frame in which the conventional IMU is placed. Left: General setting. Two sensor frames, **sx** and **sy**, are depicted, with each one sensitive for a single spatial dimension, indicated by a wavy line. A third frame, **sz**, may be placed with the sensitive axis aligned along the $\mathbf{b}_3$ direction. Right: Multi-axis scheme. By using a single source and three different laser beam directions aligned with the axes of the **s** frame, acceleration measurements on all spatial axes can be realized.

The differential equations are solved by integration to determine the atom positions at times $t = T$ and $t = 2T$ and to calculate the phase via Equation (4). Unless otherwise stated, all parameters are time-dependent.

3.1.2 | Consideration of Spatial Displacements Between Sensors

The accelerations $\mathbf{f}_{ib}^{b}$ and turn rates $\boldsymbol{\Omega}_{ib}^{b}$ are now given in a different system **b**, i.e., the body frame with the origin at the center of the IMU. This arrangement results in a spatial distance to the s-frame in which the quantities must be transformed, i.e., a lever arm $\mathbf{x}_{b,sj}^{b}$, cf., Figure 3. As an example, for a very simplistic and general design of a three-dimensional atomic sensor system, it can be assumed that there are three atomic interferometers with frames **sx**, **sy**, and **sz**, each with a sensitive axis in one of the spatial dimensions. The transformations of specific forces in this case are as follows:

$$\mathbf{f}_{i,sj}^{sj} = \mathbf{f}_{i,b}^{sj} + \mathbf{f}_{b,sj}^{sj} = \mathbf{C}_{b}^{sj}\mathbf{f}_{ib}^{b} - \mathbf{C}_{b}^{sj}\boldsymbol{\Omega}_{ib}^{b}(\boldsymbol{\Omega}_{ib}^{b}\mathbf{x}_{b,sj}^{b}) - \mathbf{C}_{b}^{sj}\dot{\boldsymbol{\Omega}}_{ib}^{b}\mathbf{x}_{b,sj}^{b} \tag{7}$$

The fictitious forces resulting from the transformation are expressed in the centrifugal term $\boldsymbol{\Omega}_{ib}^{b}(\boldsymbol{\Omega}_{ib}^{b}\mathbf{x}_{b,sj}^{b})$ and the Euler term $\dot{\boldsymbol{\Omega}}_{ib}^{b}\mathbf{x}_{b,sj}^{b}$, which results from angular accelerations of the frame. The sensor frames and body frame are all connected to a rigid platform; thus, there is no change in the distance $\mathbf{x}_{b,sj}^{b}$, and no Coriolis term $\boldsymbol{\Omega}_{ib}^{b}\dot{\mathbf{x}}_{b,sj}^{b}$ needs to be considered. This same rigid platform argument allows us to set the specific force *between* both frames to zero, $\mathbf{f}_{b,sj}^{sj} = \mathbf{0}$. A rotation $\mathbf{C}_{b}^{sj}$ between the two systems, resembling sensor misalignment, can be included.

The transformation of the turn rates is straightforward:

$$\boldsymbol{\Omega}_{i,sj}^{sj} = \boldsymbol{\Omega}_{i,b}^{sj} + \boldsymbol{\Omega}_{b,sj}^{sj} = \mathbf{C}_{b}^{sj}\boldsymbol{\Omega}_{ib}^{b} \tag{8}$$

In analogy to the forces, the rigid platform allows no relative rotation $\boldsymbol{\Omega}_{b,sj}^{sj}$ between the sensors and body frame, and thus, $\boldsymbol{\Omega}_{b,sj}^{sj} = \mathbf{0}$.

3.1.3 | Multi-Axis Model

It is assumed that all three CAI sensors use a single atomic source, as displayed in Figure 3, cf., Gersemann et al. (2020); thus, a single sensor frame **s** is sufficient. Furthermore, the misalignment between the **s** and **b** frames is assumed to be zero, and hence, $\mathbf{C}_{b}^{s}$ equals **I**, the identity matrix.

This multi-axis CAI model has three sensitive axes, which are considered in the model by their respective $\mathbf{k}^{s}$-vector. For example, for the interferometer sequence in the x direction, the vector reads $\mathbf{k}^{s} = [k_x, 0, 0]^{T}$, with k_x as the respective effective wave number. The coordinate center and the starting position of the atoms in each direction are identical. Note that in this multi-axis CAI, an initial splitter pulse is applied immediately before the Mach–Zehnder sequence, which divides the initial wave packet into two counter-propagating ensembles in order to differentiate between phase shifts based on linear acceleration and those based on rotation. This approach affects the initial velocity $\mathbf{v}_{sa}^{s}$ and will be important in Section 3.3.

According to Equation (4), the phase shift ϕ^{s} depends on the position $\mathbf{x}^{s}$ of the atoms in the s-frame. We can state the following:

$$\mathbf{x}^s = \mathbf{x}^s_{acc} + \mathbf{x}^s_{rot} + \mathbf{x}^s_{mix} \tag{9}$$

with the single position terms caused by linear acceleration $\mathbf{x}^s_{acc}$, rotation $\mathbf{x}^s_{rot}$, and effects of a changing rotation vector during the integration interval $\mathbf{x}^s_{mix}$ now explained in detail.

Acceleration

The position of the atoms in the laser frame **s**, as measured by a conventional accelerometer in the b-frame, is calculated as follows:

$$\mathbf{x}^s_{acc} = \int_0^t \int \left[-\mathbf{f}^s_{ib} + \mathbf{g}^s + \boldsymbol{\Omega}^s_{ib}(\boldsymbol{\Omega}^s_{ib}\mathbf{x}^s_{bs}) + \dot{\boldsymbol{\Omega}}^s_{ib}\mathbf{x}^s_{bs} \right] dt^2 \tag{10}$$

In the position shift caused by linear accelerations, three terms are involved in addition to gravity $\mathbf{g}^s$: the specific forces $\mathbf{f}^s_{ib}$ measured by the conventional accelerometer, the centrifugal term $\boldsymbol{\Omega}^s_{ib}(\boldsymbol{\Omega}^s_{ib}\mathbf{x}^s_{bs})$ due to the lever arm, and the Euler term $\dot{\boldsymbol{\Omega}}^s_{ib}\mathbf{x}^s_{bs}$ resulting from a change in turn rate.

Rotation

The atom position shift based on a rotation of the s-frame results from the Coriolis term alone:

$$\mathbf{x}^s_{rot} = \int_0^t \int \left[2\boldsymbol{\Omega}^s_{ib}\mathbf{v}^s_{s,a} \right] dt^2 \tag{11}$$

Coning

The presence of turn rates during the measurement interval leads to a change in orientation vector of the s-frame, which must be considered. An additional coning/sculling mixture term appears, cf., Savage (1998), which will subsequently be labeled with the subscript *mix*. The position of the atoms in the laser frame is then as follows:

$$\mathbf{x}^s_{mix} = \int_0^t \int \left[\int_0^t \boldsymbol{\Omega}^s_{ib} dt \right] \left[\mathbf{g}^s - \mathbf{f}^s_{ib} + \boldsymbol{\Omega}^s_{ib}(\boldsymbol{\Omega}^s_{ib}\mathbf{x}^s_{bs}) + \dot{\boldsymbol{\Omega}}^s_{ib}\mathbf{x}^s_{bs} \right] dt^2 \tag{12}$$

Note that the same fictitious force terms, namely the centrifugal and Euler terms, apply as in the linear acceleration case. The difference here is that the whole term is rotated by the relative change in orientation $\int \boldsymbol{\Omega}^s_{ib} dt$.

Higher-Order Terms

The wave packet is potentially affected in the presence of gravity gradients or gravitational waves, which leads to higher-order phase shift terms with respect to

the integration time (Antoine & Borde, 2003; Bongs et al., 2006). For the terrestrial navigation case considered herein and the often limited dimensions of CAI vacuum chambers, the interrogation time T is comparably short, typically in the range of 10–25 ms. Thus, higher-order terms only have a diminishing effect in the face of terms resulting from rotation and linear acceleration and, consequently, can be neglected.

This situation changes drastically in space applications (Trimeche et al., 2019), where large interrogation times of several seconds are achievable and gravity gradients as well as higher-order terms can no longer be ignored.

3.2 | Evaluation of the Atom Strapdown Phase Prediction

To evaluate the atom strapdown method, this technique is compared with a second method to extract the interferometer phase: the convolution of acceleration sensor signals with the interferometer sensitivity function. This method is a common way to hybridize the signals of conventional sensors with the atom interferometer response and is used by different groups, e.g., Richardson et al. (2020), Cheiney et al. (2018), and Zahzam et al. (2022). First, this method is briefly summarized. Then, the predicted phase shift of the atom strapdown method and the convolution are compared based on an experimental data set Richardson et al. (2020). In that experiment, the acceleration data of the sensor frame are measured by an optomechanical resonator (OMR) attached to the retroreflection mirror of the interferometer. This sensor is a mere prototype, and its characteristics are only briefly stated.

Phase Reconstruction by Convolution

To reconstruct the atom interferometer response that has been distorted because of acting ambient ground vibrations, the OMR signal is convolved with the acceleration sensitivity function $f(t)$ of the atom interferometer, given in Equation (13) and shown in Figure 4. This convolution is then integrated over the interferometer duration to calculate the corresponding phase correction value for that particular atom interferometer shot, as shown in Equation (14):

$$f(t)=\begin{cases}\frac{1}{\Omega_{eff}}\left(1-\cos(\Omega_{eff}t)\right) & \text{for} \quad 0<t\leq\tau\\ t+\frac{1}{\Omega_{eff}}-\tau & \text{for} \quad \tau<t\leq T+\tau\\ T+\frac{1}{\Omega_{eff}}\left(1-\cos(\Omega_{eff}(t-T))\right) & \text{for} \quad T+\tau<t\leq T+3\tau\\ 2T+3\tau+\frac{1}{\Omega_{eff}}-t & \text{for} \quad T+3\tau<t\leq 2T+3\tau\\ \frac{1}{\Omega_{eff}}\left(1-\cos(\Omega_{eff}(t-2T))\right) & \text{for} \quad 2T+3\tau<t\leq 2T+4\tau\\ 0 & \text{for} \quad \textit{otherwise}\end{cases} \tag{13}$$

Here, Ω_{eff} is the effective Rabi frequency, τ is the laser pulse duration, and T is the interrogation time:

$$\Phi_{vib}=k_{eff}\int_{-\infty}^{\infty}f(t)a_{vib}(t)dt \tag{14}$$

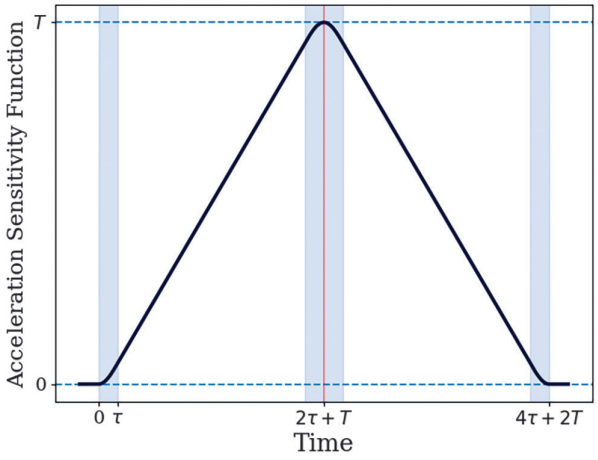

FIGURE 4 Acceleration sensitivity function of the atom interferometer according to Equation (13)

The OMR has a sensitivity on the order of 10^{-5} m/s^2 for frequencies above 10 Hz; at lower frequencies, 1/f noise dominates. Therefore, the OMR is capable of suppressing ambient vibrational noise for interferometers with lower integration times, with a maximum limit of 10 ms for good fringe reconstruction. This limitation arises because interferometers with lower T have a higher corner cut-off frequency, which is given by $1/2T$; therefore, higher-frequency vibrations will be capable of inducing noise to the interferometer. Beyond an interrogation time of 10 ms, the fringe reconstruction performance obtained via the OMR signal declines because of its poor low-frequency performance.

The acceleration data were acquired at a rate of 100 kHz throughout the interferometer duration, which spans $T_{MZ} = 0.02003$ s. Consequently, for each shot of the atom interferometer, 2003 acceleration measurement samples are integrated over the interferometer duration in the strapdown in order to calculate the atom position in the sensor frame by using the equations in Section 3.1.3. The positions at the times of the atom–laser interactions are then used in Equation (4) to compute the phase shift. The Earth turn rate at the local latitude, 52.38°, is used as input for Ω_{is}^{s}.

Evaluation

The resulting phase shifts from both methods show good agreement, cf., Figure 5. However, a relatively constant offset of approximately 0.04% is visible, as well as occasional spikes of up to 0.186%. The largest difference during the whole experiment with over 17000 CAI shots is approximately 2%.

One possibility for the deviation lies in the beam splitter pulse durations, which are not yet considered in the atom strapdown method. The two state splitter pulses each have a duration of 7.5 μs, while the duration of the mirror pulse is twice as long, leading to a total of 30 μs. During these pulses, the sensitivity of the interferometer regarding the inertial quantity changes, following a sinusoidal pattern, cf., Equation (13). Because of the 100-kHz accelerometer data rate, approximately 3–5 of the 2003 data points are integrated differently in the two methods.

Finally, we include some general remarks on the two methods: The convolution technique uses the sensitivity of the atom interferometer with respect to changes in the phase shift, which is then further related to the sensitivity to the acceleration of the sensor frame.

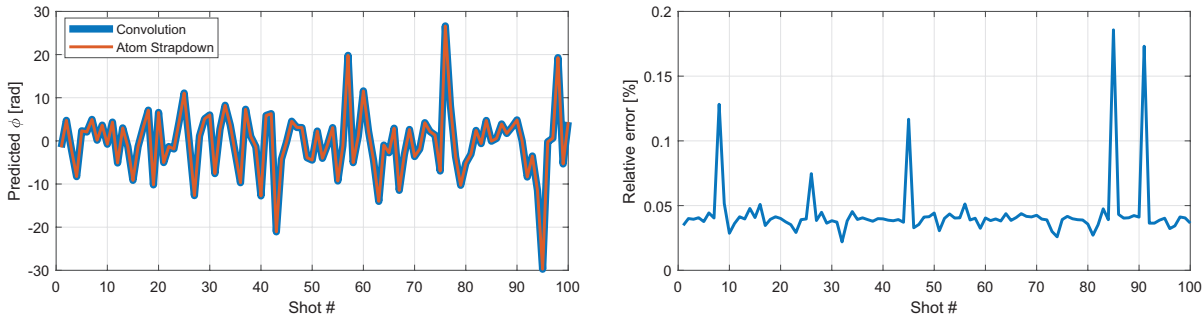

FIGURE 5 Comparison of the two phase shift calculation methods
Left: The two results generally agree very well, and a deviation is hardly visible. Right: The relative error, i.e., the difference between the results of the methods divided by the half-sum of both results, reveals a nearly constant systematic offset of approximately 0.04%, whereas larger spikes occur for some shots. Depicted are the first 100 CAI measurement intervals typical for a data set of 17440 measurements in total.

In the atom strapdown method, the position of the atoms is calculated explicitly. However, the phase shift in Equation (1), which uses the atom position as input, originates from the sensitivity of the atom interferometer response. Thus, the convolution method can be seen as a more specialized and slim way of combining signals of different sensors with the CAI measurement, whereas the atom strapdown method is a more general approach, allowing the consideration of arbitrary target frames.

The new method can be further used to include different motion models and dynamics in the differential equation system. Furthermore, different sensors could be utilized to predict the atom position, for example, odometry from car wheels or visual sensors.

3.3 | Implementation of Phase Prediction in a Hybrid Filter

Thus far, the atom strapdown method has been introduced as a way to predict the phase shift of an atom interferometer in an arbitrary sensor frame. The general steps for implementing the phase shift prediction in a filter framework (see Figure 6) have been sketched in prior works, e.g., Tennstedt & Schön (2021). Some important aspects are now repeated and explained, including the adaption of the measurement model, as the new dynamic equations need some special care.

It is worth stressing the clear differentiation between the kinematic state of the moving platform calculated in the IMU strapdown, i.e., the position $\mathbf{x}^n_{eb}$ and velocity $\mathbf{v}^n_{eb}$ of the body frame (index b) with respect to the Earth frame (index e) as well as the attitude $\mathbf{C}^n_b$ in a target navigation frame (superscript n), from the kinematic state of the atom wave packet in the sensor frame (atom strapdown). The parameters that are used in both systems are the bias of the accelerations $\mathbf{b}_a$ and angular rate measurements $\mathbf{b}_g$. The kinematic state of the wave packet changes with each new measurement cycle; thus, it is not necessary to keep track of these states beyond the corresponding measurement interval. Consequently, the state vector of the filter inherits the kinematic state of the platform with the IMU bias as a state augmentation:

$$\mathbf{x} = [\mathbf{x}^n_{eb}, \mathbf{v}^n_{eb}, \mathbf{b}_a, \mathbf{b}_g]^T \tag{15}$$

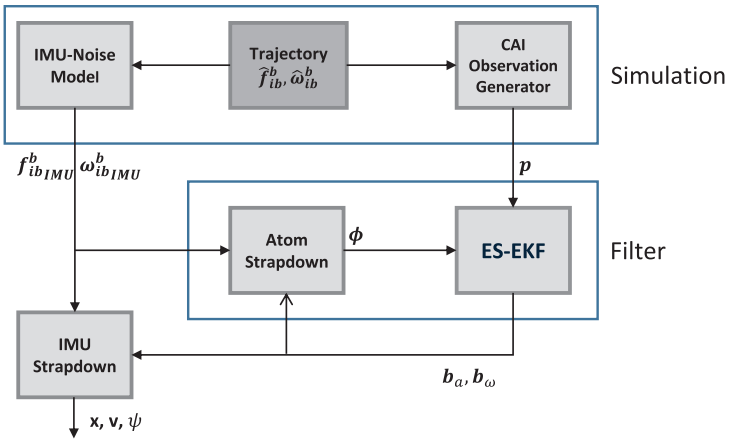

FIGURE 6 Integration of the atom strapdown method in a filter and simulation framework The CAI response (phase shift ϕ) is predicted by the conventional IMU data and fused with the actual CAI observation p in the error state extended Kalman filter (ES-EKF) to estimate the bias of the IMU sensors.

With this design decision, the filter innovation, which is based on the atom phase shift model, can also be used to correct the kinematic state of the platform, due to coupling with the bias in the system model. The corresponding transition matrix $\mathbf{F}$ over the course of a system time step Δt is as follows:

$$\mathbf{F} = \begin{pmatrix} \mathbf{I}_3 & \mathbf{I}_3\Delta t & \frac{1}{2}\mathbf{C}_b^n\Delta t^2 & \mathbf{0}_3 \\ \mathbf{0}_3 & \mathbf{I}_3 & \mathbf{C}_b^n\Delta t & \mathbf{0}_3 \\ \mathbf{0}_3 & \mathbf{0}_3 & \mathbf{I}_3 & \mathbf{0}_3 \\ \mathbf{0}_3 & \mathbf{0}_3 & \mathbf{0}_3 & \mathbf{I}_3 \end{pmatrix} \tag{16}$$

The uncertainties for the accelerometers $\mathbf{w}_a$ and gyroscopes $\mathbf{w}_g$ are modeled as white noise with respective variances σ_n^2 and random walk processes. The variance σ_{rw}^2 of the latter is modeled by an integrator with white noise $w_{rw,in}$ as input, sampled from a Gaussian distribution with variance $\sigma_{rw,in}^2\Delta t$. For each individual axis and sensor, the process reads as follows:

$$w_{rw}(t+\Delta t) = w_{rw}(t) + w_{rw,in}(t) \tag{17}$$

The processes are combined in the system perturbation vector $\mathbf{w} = [\mathbf{w}_a, \mathbf{w}_g]^T$ and affect the bias of the accelerations and angular rates. Hence, the perturbation input $\mathbf{B}$ matrix reads as follows:

$$\mathbf{B} = \begin{pmatrix} \mathbf{0}_3 & \mathbf{0}_3 \\ \mathbf{0}_3 & \mathbf{0}_3 \\ \mathbf{I}_3 & \mathbf{0}_3 \\ \mathbf{0}_3 & \mathbf{I}_3 \end{pmatrix} \tag{18}$$

where the covariance matrix is given as follows:

$$\mathbf{Q}_w = \begin{pmatrix} \sigma_a^2\mathbf{I}_3 & \mathbf{0}_3 \\ \mathbf{0}_3 & \sigma_g^2\mathbf{I}_3 \end{pmatrix} = \begin{pmatrix} (\sigma_{a,n}^2 + \sigma_{a,rw,in}^2\Delta t)\mathbf{I}_3 & \mathbf{0}_3 \\ \mathbf{0}_3 & (\sigma_{g,n}^2 + \sigma_{g,rw,in}^2\Delta t)\mathbf{I}_3 \end{pmatrix} \tag{19}$$

The discrete time process noise matrix with subscript k indicating the time step $t \rightarrow t + \Delta t$ can then be assembled:

$$\mathbf{Q}_k = \int_t^{t+\Delta t} \mathbf{F}\mathbf{B}\mathbf{Q}_w\mathbf{B}^T\mathbf{F}^T dt \tag{20}$$

The remaining equations follow that of a regular EKF with error states, as described in Tennstedt et al. (2021). Thus, at the filter step at time step k, the total state $\hat{\mathbf{x}}_k$ is updated with the estimated error state $\delta\hat{\mathbf{x}}_k$:

$$\hat{\mathbf{x}}_k^+ = \hat{\mathbf{x}}_k^- + \delta\hat{\mathbf{x}}_k^+ \tag{21}$$

The superscript − denotes a predicted state, whereas + denotes a filtered state. At each filter update, the predicted error state is always initialized as zero; hence, the filtered error state is essentially the difference between the CAI observation $\mathbf{p}_k$ and the predicted observation $\mathbf{h}(\hat{\mathbf{x}}_k^-)$, weighted by the Kalman gain $\mathbf{K}_k$:

$$\delta\hat{\mathbf{x}}_k^+ = \mathbf{K}_k \cdot (\mathbf{p}_k - \mathbf{h}(\hat{\mathbf{x}}_k^-)) \tag{22}$$

The observation model $\mathbf{h}$ of the CAI is based on the phase prediction obtained from the IMU data. The acceleration measurement of the IMU, $\mathbf{f}_{ib}^b$, must be adapted in order to include a potential deviation $\mathbf{b}_a$, i.e., bias, from the true acceleration value $\tilde{\mathbf{f}}_{ib}^b$:

$$\mathbf{f}_{ib}^b = \tilde{\mathbf{f}}_{ib}^b + \mathbf{b}_\mathbf{a} \tag{23}$$

The analytical CAI observation equation per axis is the transition probability p:

$$p = \frac{1}{2}\left(1 + \cos(\phi_0 + \phi + \delta\phi)\right) \tag{24}$$

where ϕ_0 is the steered laser phase and ϕ is the phase shift prediction from the IMU data. Readout contrast and offset of the actual signal are not considered in the scope of this paper. In fact, only the contrast affects the sensitivity in a real application.

The steered phase ϕ_0 is set such that the sum of ϕ_0 and ϕ equals $\frac{\pi}{2}$ in order to maximize the sensitivity with respect to the additional bias-induced phase shift $\delta\phi$.

The derivative of Equation (24) with respect to the accelerometer bias reads as follows:

$$\frac{\partial p}{\partial \mathbf{b}_a}\Big|_{\phi_0+\phi=\frac{\pi}{2}} = -\frac{1}{2}\sin(\frac{\pi}{2} + \delta\phi)\frac{\partial\delta\phi}{\partial \mathbf{b}_a} \tag{25}$$

In the limit of $\delta\phi \rightarrow 0$, we obtain the following:

$$\lim_{\delta\phi\rightarrow 0}\frac{\partial p}{\partial \mathbf{b}_a} = -\frac{1}{2}\sin(\frac{\pi}{2})\frac{\partial\delta\phi}{\partial \mathbf{b}_a} = -\frac{1}{2}\frac{\partial\delta\phi}{\partial \mathbf{b}_a} \tag{26}$$

The observation matrix $\mathbf{H}_a$ for the acceleration bias is then written as follows:

$$\mathbf{H}_a = \frac{\partial p}{\partial \mathbf{b}_a} = -\frac{1}{2}(\mathbf{k}^s)^T T^2 - \frac{1}{2}(\mathbf{k}^s)^T \mathbf{\Omega}_{ib}^s T^3 \tag{27}$$

Only the acceleration and mixed term, cf., Equation (10) and Equation (12), respectively, are sensitive for an acceleration bias. Because of the skew-symmetric matrix $\mathbf{\Omega}_{ib}^s$, the second term is non-zero only if the angular rate in the direction of

the respective perpendicular axes is non-zero. This result is in line with the prior statement that the phase shift on a particular sensitive CAI axis is only affected by rotations perpendicular to the axis.

The observation matrix $\mathbf{H}_g$ for the gyroscope bias follows a similar pattern. The IMU gyroscope measurement $\boldsymbol{\omega}_{ib}^b$ consists of the true angular rates $\tilde{\boldsymbol{\omega}}_{ib}^b$ and the bias $\mathbf{b}_g$:

$$\boldsymbol{\omega}_{ib}^b = \tilde{\boldsymbol{\omega}}_{ib}^b + \mathbf{b}_g \tag{28}$$

The derivative of Equation (24) with respect to the gyroscope bias is as follows:

$$\frac{\partial p}{\partial \mathbf{b}_g}|_{\phi_0+\phi=\frac{\pi}{2}} = -\frac{1}{2}\sin(\frac{\pi}{2}+\delta\phi)\frac{\partial \delta\phi}{\partial \mathbf{b}_g} \tag{29}$$

As before, the limit of $\delta\phi \to 0$ gives the following:

$$\lim_{\delta\phi\to 0}\frac{\partial p}{\partial \mathbf{b}_g} = -\frac{1}{2}\sin(\frac{\pi}{2})\frac{\partial \delta\phi}{\partial \mathbf{b}_g} = -\frac{1}{2}\frac{\partial \delta\phi}{\partial \mathbf{b}_g} \tag{30}$$

The observation matrix $\mathbf{H}_g$ for the gyroscope bias results in a rather extensive expression:

$$\begin{aligned}\mathbf{H}_g = \frac{\partial p}{\partial \mathbf{b}_g} = &\frac{1}{2}(\mathbf{k}^s)^T[(\Omega_{ib}^s \mathbf{x}_{bs}^s)\times]T^2 + \frac{1}{2}(\mathbf{k}^s)^T\Omega_{ib}^s[\mathbf{x}_{bs}^s\times]T^2 + (\mathbf{k}^s)^T[\mathbf{v}_{sa}^s\times]T^2 \\ &+\frac{1}{2}(\mathbf{k}^s)^T[\mathbf{f}_{ib}^s\times]T^3 + \frac{1}{2}(\mathbf{k}^s)^T[\Omega_{ib}^s(\Omega_{ib}^s\mathbf{x}_{bs}^s)\times]T^3 + \frac{1}{2}(\mathbf{k}^s)^T\Omega_{ib}^s[(\Omega_{ib}^s\mathbf{x}_{bs}^s)\times]T^3 \\ &+\frac{1}{2}(\mathbf{k}^s)^T\Omega_{ib}^s(\Omega_{ib}^s[\mathbf{x}_{bs}^s\times])T^3 + \frac{1}{2}(\mathbf{k}^s)^T[(\dot{\Omega}_{ib}^s\mathbf{x}_{bs}^s)\times]T^3\end{aligned} \tag{31}$$

The first two terms come from the derivative of the centrifugal term with respect to the gyroscope bias. The term $(\mathbf{k}^s)^T[\mathbf{v}_{sa}^s\times]T^2$ resembles the Coriolis term observed for the atoms in a rotating s-frame. This term scales with the atom velocity. The fourth term $\frac{1}{2}(\mathbf{k}^s)^T[\mathbf{f}_{ib}^s\times]T^3$ results from the partial derivative of the mixed term, which scales with the linear accelerations. Terms five to seven are produced by the product rule when differentiating the centrifugal term between the b- and s-frame. The final Euler term including the angular acceleration $\dot{\Omega}_{ib}^s$ is not considered for the EKF measurement linearization in the frame of this work because of the inaccessibility of these values. The angular accelerations can be acquired by either numerical differentiation of the turn rates or state vector augmentation when using at least three conventional IMUs. However, the first method is rather inaccurate because of the differentiation of gyroscope white noise in the signal, whereas the second method may be evaluated in a future study.

The complete observation matrix $\mathbf{H}$ can now be constructed:

$$\mathbf{H} = \begin{pmatrix}\mathbf{0} & \mathbf{0} & \mathbf{H}_a & \mathbf{H}_g\end{pmatrix} \tag{32}$$

Thus far, the observation equation and matrices in the s-frame have been stated for an arbitrary CAI observation on a single sensitive axis as defined by the wave vector $\mathbf{k}^s$. In the six-degree-of-freedom case, there are now two measurements per spatial axis at a time in order to differentiate between angular rates and linear accelerations. In this case, the observation vector reads $\mathbf{p} = [p_x^A, p_y^A, p_z^A, p_x^B, p_y^B, p_z^B]^T$, where the superscripts A and B refer to anti-parallel propagating wave packets after the initial separation split. The individual phase shifts are predicted

for each observation independently; thus, for three sensitive CAI axes with two counter-propagating wave packets, there is a total of six different predicted atom wave packet states.

For now, it is assumed that the interferometers on all axes perform measurements at the same time. Thus, the observation matrices are individually computed according to Equations (27) and (31) with the respective $\mathbf{k}^s$ and $\mathbf{v}^s_{sa}$ and are finally added together to produce a single update step.

4 | RESULTS AND DISCUSSION

4.1 | Impact of Dynamics on Phase Shift Terms

Setting

We now consider a hybrid solution between a conventional IMU and the CAI according to the *multi-axis scheme*. The previous equations revealed a number of fictitious force terms when the IMU measurement is transformed from the b-frame to the sensor frame. To evaluate the impact of different dynamics on the single phase shift terms, a trajectory with a constant velocity of 1 m/s in the driving direction $\mathbf{s}_1$ as well as one period of a sinusoidal changing yaw rate with an amplitude of 0.05 rad/s is simulated. With these settings, it is possible to apply an angular rate and angular acceleration on $\mathbf{s}_3$ and an accelerations in the $\mathbf{s}_2$ direction and thus excite all phase shift terms.

The goal is to determine to which order of magnitude the single terms affect the phase shift of the interferometer. Afterwards, the effect of the most dominant terms on the error phase shift in the case of an IMU bias is evaluated depending on the sensor distance $\mathbf{x}^s_{bs}$.

Results

The results in Figure 7 show that in the *forward direction*, the rotation term is dominant. Whereas the Euler and centrifugal terms of the acceleration as well as the mixed term generally scale with the distance between the b- and s-frames, the largest effect arises from the centrifugal term. In the *right direction*, the largest impact results from the lateral accelerations of the trajectory. However, the angular accelerations are scaled by the lever arm as well, which leads to an increased Euler term that surpasses even the lateral accelerations in parts of the simulation when the lever arm is set to 1 m, e.g., at $t = 25$ s. Regarding the mixed terms, the effect is generally quite small. In fact, the mixed term resembles the transformation terms of the linear accelerations, scaled by the integrated angular rates. Thus, for most terrestrial applications, these terms are smaller than the centrifugal and Euler terms from the transformation of the linear acceleration alone.

Next, we focus on the effect of the lever arm on the dynamic terms. In contrast to the prior example, the error of the predicted phase in the case of a bias in the accelerations and angular rates is now examined. Instead of a time-dependent trajectory, only a *slice* of the trajectory with the dynamics at an exact time is given. The phase error in this situation is evaluated based on the size of the lever arm, where $\mathbf{x}^s_{bs} = [\ell, -\ell, 0]^T$ is varied in the interval $\ell \in [0, 1]$ m on an equidistant scale.

The parameters are set as follows, according to the maximum values that can be expected for typical maneuvers. A constant angular rate $\boldsymbol{\omega}^s_{ib} = [0.1, 0.1, 0.5]^T$ rad/s and acceleration $\mathbf{f}^s_{ib} = [-3, 4, 5]^T$ m/s^2 represent the dynamic situation. The

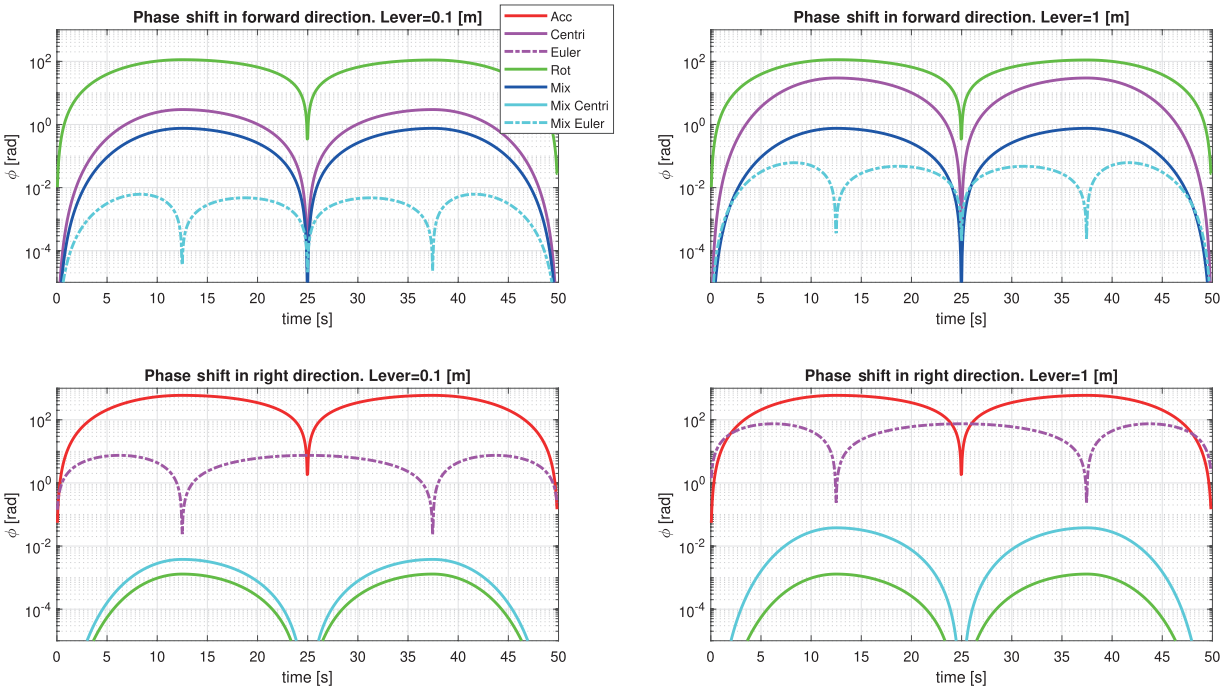

FIGURE 7 Impact of the different transformation terms on the CAI phase shift in the forward (top panels) and right (bottom panels) direction
The figures show the magnitude of the phase shift. A logarithmic scale is chosen to facilitate the separation of the single dynamic terms, as the *mixed* terms are comparably small. Similarly, the y-axis is limited to the range of $[10^{-5}, 10^{3}]$ rad to avoid unfavorable scaling. As expected from the dynamic equations, the lever arm $\mathbf{x}_{bs}^{s} = [\ell, 0, 0]^{T}$, where ℓ is the value indicated in the title of each subfigure, linearly scales the centrifugal (*Centri*) and Euler parts of both the acceleration and mixture term.

angular rate and angular acceleration for the mixture Euler term are scaled down by a factor of $1/\sqrt{2}$ to account for being normally phase-shifted by 90 degrees with respect to each other, as Figure 7 demonstrates in the *right direction* for the example of the Euler and acceleration terms.

The constant biases of the acceleration and angular rate signals are defined as $b_a = 10^{-4}$ m/s^2 and $b_g = 3 \cdot 10^{-5}$ rad/s on all axes.

The interrogation time and wave numbers are $T = 25$ ms and $k_{x,y,z} = 4\pi/780$ nm, respectively. The initial atom velocity $\mathbf{v}_{sa}^{s} = [0, 0.096, 0]^{T}$ m/s is summed with the integrated linear accelerations $\mathbf{f}_{ib}^{s} \cdot 2T$ in order to emulate the largest atom velocity to be expected.

As shown in Figure 8, the linear acceleration and the rotation in the corresponding direction are naturally independent of the lever arm. The acceleration has a relatively large impact, which is caused by the comparably large accelerometer bias. The two terms that show the greatest scaling with the magnitude of the lever arm are the centrifugal and Euler terms. This trend matches the results in Figure 7, but also shows that even a small distance of 0.4 m in any direction can surpass the dynamic range defined by the atom interferometer measurement equation.

4.2 | Impact of Dynamics on Bias Estimates

Thus far, the new algorithms have been introduced and the adaption of a hybrid filter presented. The results have indicated that the spatial displacement $\mathbf{x}_{bs}^{s}$

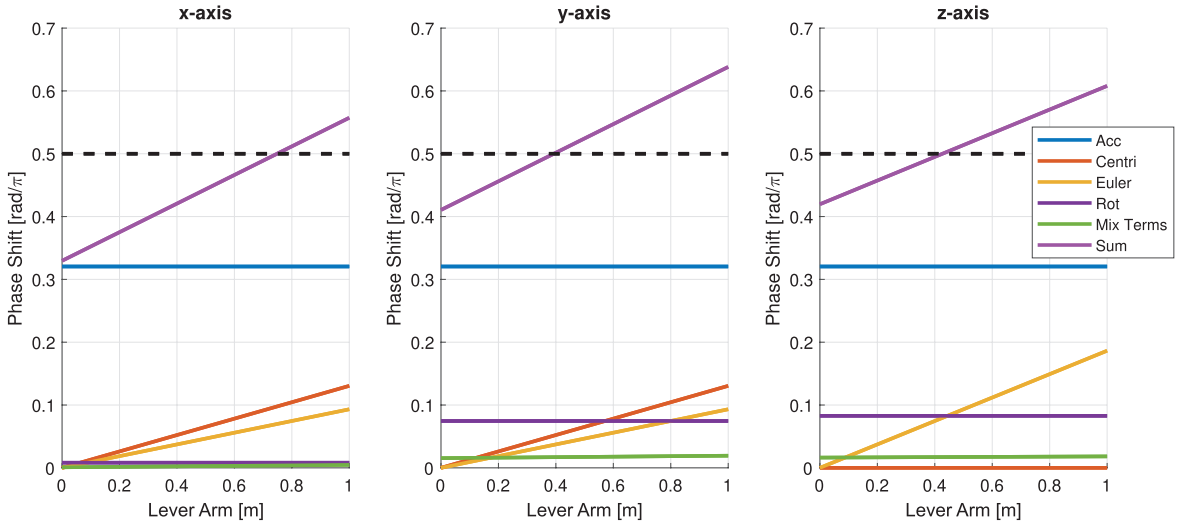

FIGURE 8 Phase shift errors induced by accelerometer and gyroscope bias depending on the spatial distance between the IMU and CAI
The dotted black line represents the maximum allowed phase shift in order to stay on one flank of the cosine signal, i.e., the maximum dynamic range of the CAI observation. The magenta line is the sum of all phase shift terms. The coning terms are combined under *Mix Terms* because of their comparably low magnitude. The lever arm range of values represents the value ℓ in $\mathbf{x}_{bs}^{s} = [\ell, -\ell, 0]^T$.

between the CAI and the IMU might lead to difficulties for the bias estimate. The correction of this bias is a crucial step in improving the hybrid navigation solution. Based on another trajectory derived from a number of different dynamic experiments (Weddig et al., 2022), the effect of the dynamics in the s-frame on the bias estimate is further investigated.

Setting

A trajectory that involves most of the maneuvers identified in the analysis of different data sets collected with IMUs during real-world measurement campaigns is simulated, cf., Figure 9. After an initial static phase, an accelerated phase follows with some minor vibrations on all axes. This phase is followed by a sliding right turn, with only the angular rate changing. Afterwards, a left turn is applied with accelerations in the $\mathbf{b}_1$ and $\mathbf{b}_2$ directions, as well as a spike in both signals at t = 26 s. The trajectory is concluded with another accelerated phase with vibrations and a small turn rate on the $\mathbf{b}_3$ axis.

The simulated IMU acceleration signal is affected by a discrete white noise process with a standard deviation of $5 \cdot 10^{-5}$ m/s^2. Additionally, a random walk process based on integrated white noise with variance $9 \cdot 10^{-10}$ m^2/s^5 is applied in order to introduce a significant drift of the signal. The gyroscope measurement consists of the angular rates with additive white noise samples with a standard deviation of $1.4544 \cdot 10^{-5}$ rad/s and a random walk process with input white noise sampled from a variance of $4 \cdot 10^{-14}$ rad^2/s^3. This measurement corresponds to the performance of a navigation-grade ringlaser gyroscope. The data rate of the simulated trajectory and the IMU is 200 Hz. The CAI is modeled with a discrete white noise process with a variance of $1 \cdot 10^{-3}$ a.u. added to the transition probability. The interrogation time is set to $T = 25$ ms, corresponding to a filter rate of $\Delta t = 2T = 50$ ms, with no dead or readout times considered. The uncertainty of the simulated CAI translates to a phase uncertainty of approximately 63 mrad or, in

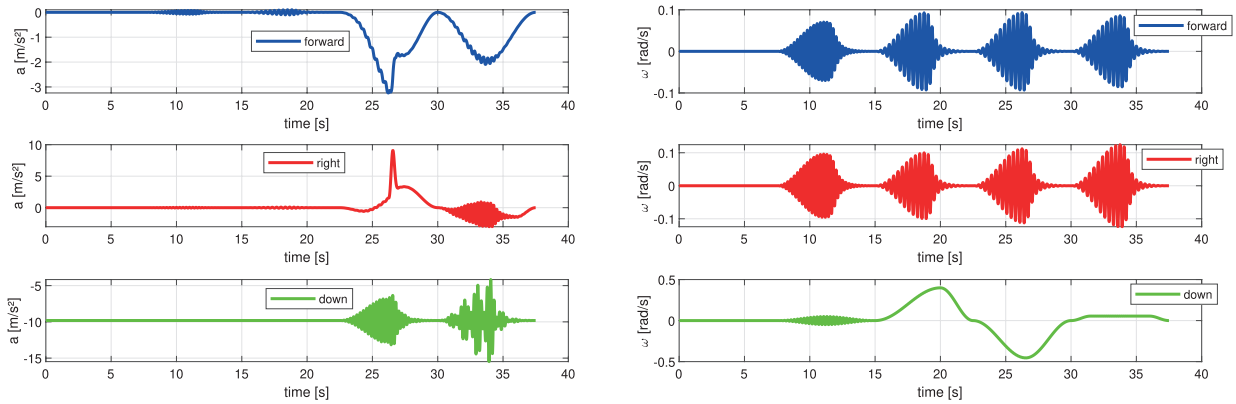

FIGURE 9 Trajectory generated from the measured data showing the accelerations (left) and rotation rates (right)
The track includes several different maneuvers of 7.5 s length each, including a stationary phase with oscillations on the different sensor axes, timed accelerations, and turn maneuvers.

conjunction with the interrogation time, an acceleration uncertainty with a standard deviation of $6.3 \cdot 10^{-6}$ m/s^2 per shot.

A spatial displacement of $\mathbf{x}_{bs}^{s} = [0, 0, 0.1]^T$ m is applied, which was selected based on the results from the previous section, where the values for $\mathbf{f}_{ib}^{b}$ and $\boldsymbol{\omega}_{ib}^{b}$ are based on the maximum amplitude of the oscillations and the bias is equal to the deviation of approximately 2σ for the respective white noise process. This distance may resemble an IMU placed directly over the atom interferometer frame. The simulation was processed in 100 different runs, in which all noise processes were sampled independently. Importantly, this number allows for the intended qualitative discussion, but is not sufficient for a statistically proven Monte-Carlo analysis, as twelve independent variables are sampled in total.

Note that in the trajectory at approximately 26 s, when the large spike in accelerations in the x and y direction occurs, the oscillation amplitude in the acceleration signal in the z direction also reaches its maximum. At the same time, the amplitude of the angular rates in x and y peaks, while a large turn rate in the z direction is present as well. According to the experiment in the previous section, it can be expected that the phase shift error resulting from this situation might be similar to or even larger than the dynamic range of the atom interferometer and thus produce an error in the filtered solution.

Results

The acceleration bias estimates, cf., Figure 10, are able to follow the noise process quite well, and the effects of the dynamics of the trajectory can hardly be seen. The increase in uncertainty over time, as reflected in the empirical standard deviation, is explained by the random walk that was added to the base signals. In the standard deviation of the gyroscope bias, two distinct peaks can be seen at approximately 26 s and 33–35 s, prominently in the x and y direction. This expected decrease in performance is also visible in the velocity $\mathbf{v}_{eb}^{n}$ state, cf., Figure 11. Although the velocity estimate of the hybrid solution is largely improved during the first 25 s with a factor of approximately 100 at best, there is a sudden increase in the error at approximately 26 s. The acceleration spikes in the trajectory scale with the accelerometer and gyroscope errors in the mixed term, leading to a comparably large phase error. At 33 s, a similar case occurs when the magnitude of the trajectory signals on all axes is at a local maximum.

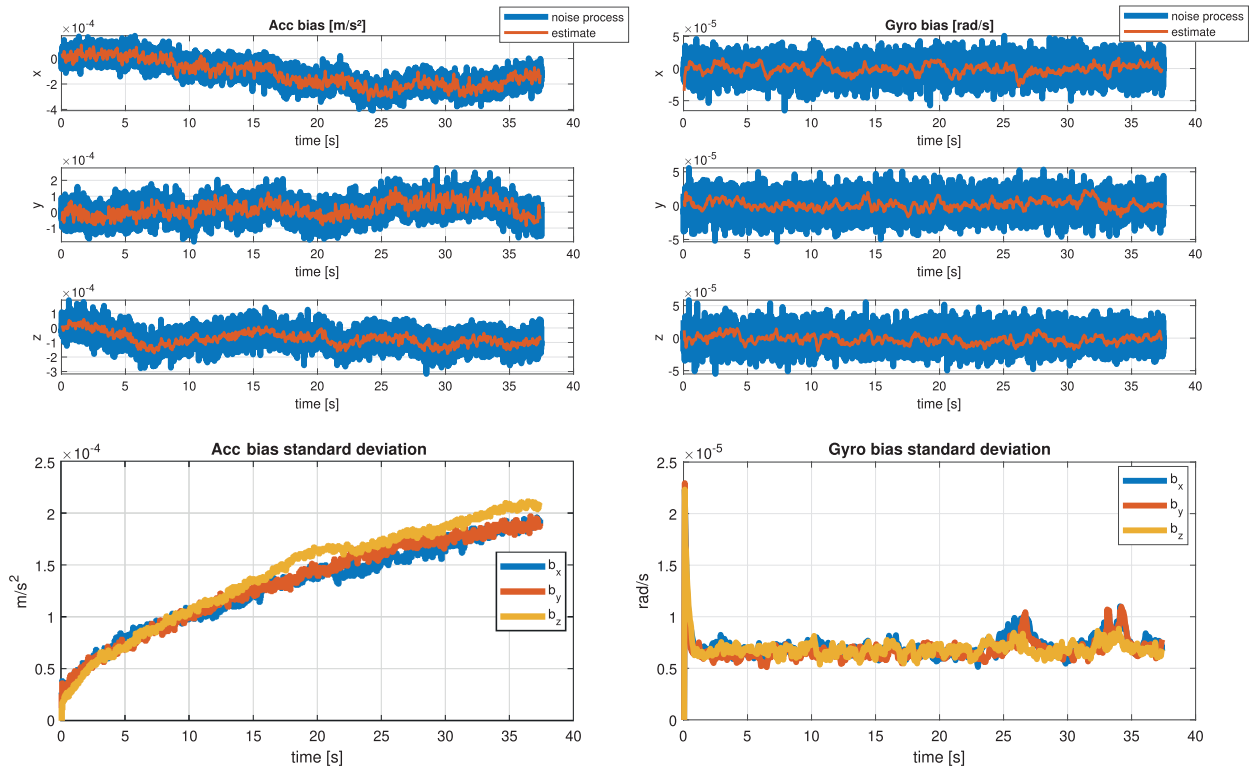

FIGURE 10 Simulation results for the estimated acceleration and gyro biases
Top panels: Acceleration and gyroscope bias (blue lines, added to the simulated reference as additive noise signal) and the estimated bias states (red lines) as an example for one of the simulated instances. Left: The acceleration bias estimate is more noisy in the x and y directions. This result is due to the fact that the spatial displacement of the IMU is only in the z direction; hence, the centrifugal term has no effect in this direction. Bottom figures: Empirical standard deviation between simulated instances for the acceleration bias estimates (left) and gyroscope bias estimates (right).

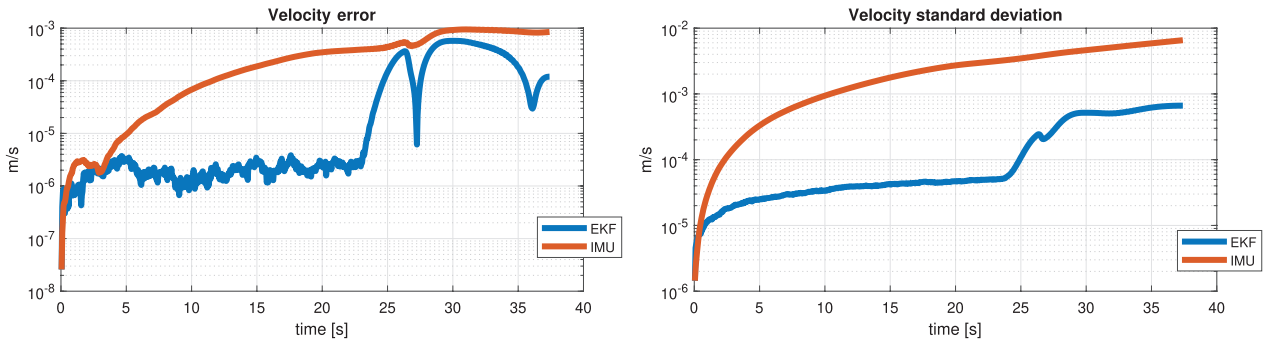

FIGURE 11 Results for the estimated velocity
Left: $\Delta \mathbf{v}_{eb}^{n}$ velocity error of the hybrid EKF solution (blue) and the IMU strapdown solution (red), with respect to the simulated ground truth. Depicted is the magnitude of the three-dimensional vector of the mean velocity error of the state instances. Right: Empirical standard deviation between the individual solutions.

In total, the error of the predicted phase was larger than $\pi/2$ in approximately 14% of the CAI measurements. This result does not necessarily imply that the target fringe is lost and the EKF update fails, as convergence to the true trajectory is generally still possible in the range of $\pm\pi$. Nevertheless, a larger linearization error occurs when the measurement sensitivities are computed in these cases, leading to a non-optimal update of the filter despite the fact that the trajectory is resolved

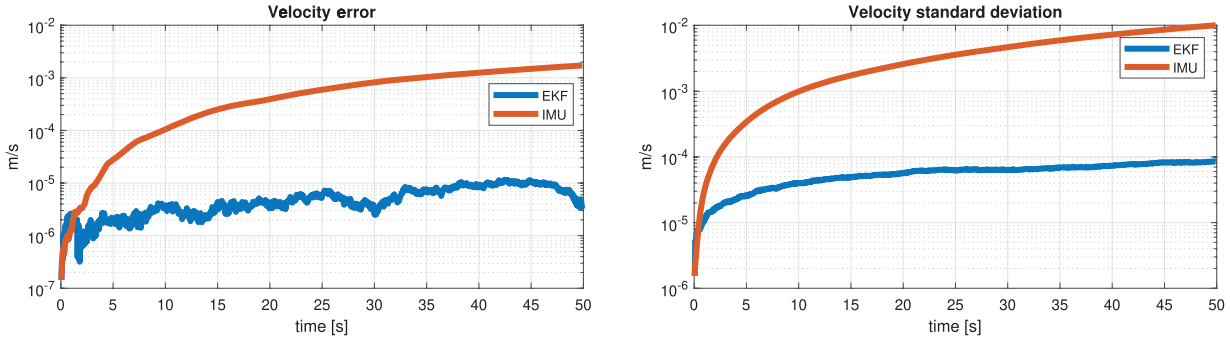

FIGURE 12 Velocity state estimates for a smooth slalom trajectory
Left: $\Delta\mathbf{v}_{eb}^{n}$ velocity error of the hybrid solution (blue) and the IMU strapdown solution (red), with respect to the simulated ground truth. Depicted is the magnitude of the three-dimensional vector. Right: Empirical standard deviation between the individual solutions.

by the IMU and the innovation $\mathbf{p}_k - \mathbf{h}(\hat{\mathbf{x}}_k^-)$ in Equation (22) is independent of the linearization.

For comparison, the results of a smooth slalom trajectory without any spikes in the signals are depicted in Figure 12. The CAI-aided EKF solution allows an improvement of over two orders of magnitude as compared with the IMU strapdown solution alone.

5 | CONCLUSION

In this paper, the atom strapdown method was introduced and explained, as well as its application for state prediction in an EKF. This hybridization technique based on a classical IMU and a CAI has two main qualities: First, it allows the phase shift of an atom interferometer to be predicted based on data from a conventional IMU. Equations were developed in a newly introduced sensor frame for the CAI. Second, this method allows one to combine measurements of an atom interferometer with conventional IMU measurements, in order to correct for IMU biases.

A comparison between the strapdown method and the hybridization technique based on convolution, developed and used in the physics community, shows that both methods deliver comparable results in the predicted CAI phase shift, while the atom strapdown method is a more general concept that allows the consideration of different dynamics and sensor systems. The methods were compared based on a static data set. Further kinematic experiments, including a one-axis CAI with controlled time-varying accelerations as well as a full six-degree-of-freedom setup, are currently planned. More detailed CAI models that include the effects of dynamics and temperature on the atoms will be investigated as well.

Taking the dynamics from real car trajectories obtained from IMU measurements, our simulations showed that it is possible to produce a valid hybrid solution of a conventional IMU and a six-axis CAI, as the trajectory states and biases are reliably estimated. Comparison with an IMU-only solution showed performance improvements of about two orders of magnitude. In the case of large signal spikes on several axes at the same time, the solution loses accuracy due to cross-coupling of different axes and due to a scale effect induced by the transformation from the b- to s-frame. Methods for identifying those situations on the fly in order to discard the CAI measurement if necessary will be investigated in future studies.

In addition, two conclusions for practical implementation can be drawn: First, the lever arm, especially between the accelerometer and the CAI, should be kept

small. The actual limit is strongly related to the IMU noise characteristics and the dynamics that are expected in individual applications. The exemplary study in Section 4.1 revealed that a distance of 40 cm between the two sensors was the maximum for the dynamic situation considered. Similar assessments could be performed for further applications. The distance is less important for the gyroscope, as the transformations from the b- to s-frame in Equation (8) show that the angular rate measurement is not affected by the lever arm. Solutions such as the OMR prototype applied directly to the retroreflection mirror of the CAI seem to provide a valid option for future hybrid accelerometer implementations, while at the same time, a high-precision gyroscope with a larger distance to the CAI could be used.

Second, the best situations for using a CAI in conjunction with an IMU might be in navigation tasks in which no spikes in the trajectory signals occur, e.g., in maneuvers with nearly constant acceleration and turn rates. Even if the EKF can cope with those situations, the best performance is achieved in smooth maneuvers. More specific applications must be examined in the future.

ACKNOWLEDGMENTS

This research was funded by the Federal Ministry for Economic Affairs and Climate Action (BMWK) due to an enactment of the German Bundestag under Grant 50RK1957 (QGyro) and 50NA2106 (QGyro+). The team also acknowledges funding from the Deutsche Forschungsgemeinschaft (DFG, German Research Foundation) under Germany's Excellence Strategy—EXC-2123 QuantumFrontiers—Project-ID 390837967.

CONFLICT OF INTEREST

The authors declare no potential conflict of interests.

REFERENCES

Antoine, C., & Borde, C. J. (2003). Quantum theory of atomic clocks and gravito-inertial sensors: An update. *Journal of Optics B: Quantum and Semiclassical Optics*, *5*(2), 199–207. https://doi.org/10.1088/1464-4266/5/2/380

Barrett, B., Gominet, P.-A., Cantin, E., Antoni-Micollier, L., Bertoldi, A., Battelier, B., Bouyer, P., Lautier, J.-M., & Landragin, A. (2014). Mobile and remote inertial sensing with atom interferometers. *Proc. of the International School of Physics "Enrico Fermi"*, *188*, 493–555. https://doi.org/10.3254/978-1-61499-448-0-493

Bongs, K., Launay, R., & Kasevich, M. (2006). High-order inertial phase shifts for time-domain atom interferometers. *Applied Physics B*, *84*(4), 599–602. https://doi.org/10.1007/s00340-006-2397-5

Cheiney, P., Fouché, L., Templier, S., Napolitano, F., Battelier, B., Bouyer, P., & Barrett, B. (2018). Navigation-compatible hybrid quantum accelerometer using a Kalman filter. *Physical Review Applied*, *10*(3), 034030. https://doi.org/10.1103/physrevapplied.10.034030

Freier, C., Hauth, M., Schkolnik, V., Leykauf, B., Schilling, M., Wziontek, H., Scherneck, H.-G., Müller, J., & Peters, A. (2016). Mobile quantum gravity sensor with unprecedented stability. *Journal of Physics: Conference Series*, *723*, 012050. https://doi.org/10.1088/1742-6596/723/1/012050

Gauguet, A., Canuel, B., Lévèque, T., Chaibi, W., & Landragin, A. (2009). Characterization and limits of a cold-atom Sagnac interferometer. *Physical Review A*, *80*(6), 063604. https://doi.org/10.1103/physreva.80.063604

Gebbe, M., Siemß, J.-N., Gersemann, M., Müntinga, H., Herrmann, S., Lämmerzahl, C., Ahlers, H., Gaaloul, N., Schubert, C., Hammerer, K., Abend, S., & Rasel, E. M. (2021). Twin-lattice atom interferometry. *Nature Communications*, *12*(1), 2544. https://doi.org/10.1038/s41467-021-22823-8

Gersemann, M., Gebbe, M., Abend, S., Schubert, C., & Rasel, E. M. (2020). Differential interferometry using a Bose-Einstein condensate. *The European Physical Journal D*, *74*(10), 203. https://doi.org/10.1140/epjd/e2020-10417-8

HosseiniArani, A., Tennstedt, B., Schilling, M., Knabe, A., Wu, H., Schön, S., & Müller, J. (2022). Kalman-filter based hybridization of classic and cold atom interferometry accelerometers for future satellite gravity missions. In *International Association of Geodesy Symposia*. 1–11. Springer, Berlin, Heidelberg. https://doi.org/10.1007/1345_2022_172

Jekeli, C. (2005). Navigation error analysis of atom interferometer inertial sensor. *NAVIGATION*, *52*(1), 1–14. https://doi.org/10.1002/j.2161-4296.2005.tb01726.x

Kasevich, M.,Weiss, D. S., Riis, E., Moler, K., Kasapi, S., & Chu, S. (1991). Atomic velocity selection using stimulated Raman transitions. *Physical Review Letters*, *66*(18), 2297–2300. https://doi.org/10.1103/physrevlett.66.2297

Kasevich, M. A., & Chu, S. (1992). Measurement of the gravitational acceleration of an atom with a light-pulse atom interferometer. *Applied Physics B*, *54*, 321–332. https://doi.org/10.1007/BF00325375

Richardson, L. L., Rajagopalan, A., Albers, H., Meiners, C., Nath, D., Schubert, C., Tell, D., Wodey, É., Abend, S., Gersemann, M., Ertmer, W., Rasel, E. M., Schlippert, D., Mehmet, M., Kumanchik, L., Colmenero, L., Spannagel, R., Braxmaier, C., & Guzmán, F. (2020). Optomechanical resonator-enhanced atom interferometry. *Communications Physics*, *3*(1), 208. https://doi.org/10.1038/s42005-020-00473-4

Roura, A., Zeller, W., & Schleich, W. P. (2014). Overcoming loss of contrast in atom interferometry due to gravity gradients. *New Journal of Physics*, *16*(12), 123012. https://doi.org/10.1088/1367-2630/16/12/123012

Savage, P. G. (1998). Strapdown inertial navigation integration algorithm design part 2: Velocity and position algorithms. *Journal of Guidance, Control and Dynamics, 21*(2)*,* 208–221. https://doi.org/10.2514/2.4242

Schubert, C., Abend, S., Gersemann, M., Gebbe, M., Schlippert, D., Berg, P., & Rasel, E. M. (2021). Multi-loop atomic Sagnac interferometry. *Scientific Reports*, *11*(1), 16121. https://doi.org/10.1038/s41598-021-95334-7

Templier, S., Cheiney, P., d'Armagnac de Castanet, Q., Gouraud, B., Porte, H., Napolitano, F., Bouyer, P., Battelier, B., & Barrett, B. (2022). Tracking the vector acceleration with a hybrid quantum accelerometer triad. *Science Advances*, *8*(45), eadd3854. https://doi.org/10.1126/sciadv.add3854

Tennstedt, B., & Schön, S. (2020). Dedicated calculation strategy for atom interferometry sensors in inertial navigation. *Proc. of the 2020 IEEE/ION Position, Location, and Navigation Symposium (PLANS),* Portland, OR. 755–764. https://doi.org/10.1109/PLANS46316.2020.9110142

Tennstedt, B., & Schön, S. (2021). Integration of atom interferometers and inertial measurement units to improve navigation performance. *Proc. of the 2021 28th Saint Petersburg International Conference on Integrated Navigation Systems (ICINS),* Saint Petersburg, Russia. 1–9. https://doi.org/10.23919/ICINS43216.2021.9470809

Tennstedt, B., Weddig, N., & Schön, S. (2021). Improved inertial navigation with cold atom interferometry. *Gyroscopy and Navigation*, *12*(4), 294–307. https://doi.org/10.1134/S207510872104009X

Trimeche, A., Battelier, B., Becker, D., Bertoldi, A., Bouyer, P., Braxmaier, C., Charron, E., Corgier, R., Cornelius, M., Douch, K., Gaaloul, N., Herrmann, S., Müller, J., Rasel, E., Schubert, C., Wu, H., & dos Santos, F. P. (2019). Concept study and preliminary design of a cold atom interferometer for space gravity gradiometry. *Classical and Quantum Gravity*, *36*(21), 215004. https://doi.org/10.1088/1361-6382/ab4548

Vermeulen, P., Lemoignc, N., Mcnoret, V., Busquet, C., Dcsruellc, B., Laurier-Gaud, J., Merlet, S., Landragin, A., Cook, A. K., & Bonvalot, S. (2018). Evaluating the performances of an operational absolute quantum gravimeter. *Proc. of the 2018 Conference on Precision Electromagnetic Measurements (CPEM 2018)*, Paris, France. 1–2. https://doi.org/10.1109/CPEM.2018.8501047

Weddig, N., Tennstedt, B., & Schön, S. (2022). Challenges for a hybrid CAI-based INS due to trajectory dynamics derived from real inertial datasets. *Proc. of the 2022 DGON Inertial Sensors and Systems (ISS),* Braunschweig, Germany. 1–20. https://doi.org/10.1109/ISS55898.2022.9926311

Weddig, N. B., Tennstedt, B., & Schön, S. (2021). Performance evaluation of a three-dimensional cold atom interferometer based inertial navigation system. *Proc. of the 2021 DGON Inertial Sensors and Systems (ISS),* Braunschweig, Germany. 1–20. https://doi.org/10.1109/ISS52949.2021.9619776

Zahzam, N., Christophe, B., Lebat, V., Hardy, E., Huynh, P.-A., Marquet, N., Blanchard, C., Bidel, Y., Bresson, A., Abrykosov, P., Gruber, T., Pail, R., Daras, I., & Carraz, O. (2022). Hybrid electrostatic/atomic accelerometer for future space gravity missions. *Remote Sensing*, *14*(14), 3273. https://doi.org/10.3390/rs14143273

How to cite this article: Tennstedt, B., Rajagopalan, A., Weddig, N.B., Abend, S., Schön, S., & Rasel, E. M. (2023). Atom strapdown: Toward integrated quantum inertial navigation systems. *NAVIGATION, 70(4)*. https://doi.org/10.33012/navi.604